



HAL
open science

Apparent Interfacial Toughness of Undoped and Photoluminescent Eu^{3+} -Doped Yttria-Stabilized Zirconia Thermal Barrier Coatings

Yankuan Liu, Etienne Copin, Sandrine Duluard, Thierry Sentenac, Zhiping P. Wang, Florence Ansart, Philippe Lours

► **To cite this version:**

Yankuan Liu, Etienne Copin, Sandrine Duluard, Thierry Sentenac, Zhiping P. Wang, et al.. Apparent Interfacial Toughness of Undoped and Photoluminescent Eu^{3+} -Doped Yttria-Stabilized Zirconia Thermal Barrier Coatings. *Journal of Thermal Spray Technology*, 2020, 29, pp.433-443. 10.1007/s11666-019-00963-0 . hal-02397243

HAL Id: hal-02397243

<https://imt-mines-albi.hal.science/hal-02397243v1>

Submitted on 6 Jan 2020

HAL is a multi-disciplinary open access archive for the deposit and dissemination of scientific research documents, whether they are published or not. The documents may come from teaching and research institutions in France or abroad, or from public or private research centers.

L'archive ouverte pluridisciplinaire **HAL**, est destinée au dépôt et à la diffusion de documents scientifiques de niveau recherche, publiés ou non, émanant des établissements d'enseignement et de recherche français ou étrangers, des laboratoires publics ou privés.

Apparent Interfacial Toughness of Undoped and Photoluminescent Eu^{3+} -Doped Ytria-Stabilized Zirconia Thermal Barrier Coatings

Yankuan Liu^{1,2} · Etienne Copin² · Sandrine Duluard³ · Thierry Sentenac² · Zhiping Wang¹ · Florence Ansart³ · Philippe Lours²

Abstract Most photoluminescence methods for the diagnostic of thermal barrier coatings (TBC) rely on the functionalization of yttria-stabilized zirconia (YSZ) with trivalent lanthanide ions. It consists in determining temperature and detecting preventively damages within the volume of the TBC prior to ceramic topcoat spallation. The latter depends on the interfacial toughness, which is an important factor to address thermal barrier coating's performance and durability. In this paper, the influence of the addition of rare earth elements (Eu^{3+}) on the interfacial toughness of TBC deposited by atmospheric plasma spray is investigated. Two types of coatings are deposited and investigated: (1) Type I: coating deposited using Eu^{3+} -doped YSZ powder (2 mol.%), (2) Type II: coating deposited using undoped YSZ powder. Both types of coatings are heat-treated at 1100 °C under isothermal conditions using different oxidation exposure times: 100, 300 and 800 h. The morphology of the interface between the topcoat (TBC) and the bond coat is analyzed by scanning electron microscopy. The apparent interfacial toughness is investigated using indentation. It is shown that the interfacial apparent toughness decreases as the oxidation exposure time increases. Concomitantly, the thickness of

the thermally grown oxide (TGO) layer between the bond coat and the topcoat increases. Results show as well that the partial substitution of Y^{3+} ions by a low amount of Eu^{3+} ions (2 mol.%) does not have influence on the microstructure and the interfacial toughness of the YSZ coatings. In addition, energy dispersive spectrometry reveals that there is no diffusion of Eu^{3+} into the TGO layer. It is therefore concluded that the use of Eu^{3+} for damage diagnostic based on photoluminescence methods will not induce any kind of degradation of the properties of TBCs.

Keywords air plasma spray · interfacial toughness · photoluminescence · thermal barrier coating · thermally grown oxide

Introduction

Thermal barrier coatings (TBCs) are widely used in components operating at high temperature such as gas turbines and aero-engines. Standard TBC systems are composed of an intermetallic bond coat such as MCrAlY ($\text{M} = \text{Ni}, \text{Co}, \text{Fe}$) or $(\text{Ni,Pt})\text{Al}$ on which is deposited a thermally insulating ceramic topcoat, made of yttria-stabilized zirconia (YSZ) in most cases. The main objective of TBCs is to protect and to insulate the underneath metallic parts in order to allow specific engine design to be run under optimized high temperatures, consequently increasing turbine efficiency. Even though the use of TBC systems results in superior performances of components (Ref 1, 2), thermal strains and stresses generated by transient thermal gradients developed during in-service thermal and mechanical cyclic exposure limit the durability of those multi-material systems, generally by initiating early

✉ Yankuan Liu
liuyankuan314@163.com

¹ Tianjin Key Laboratory of Civil Aircraft Airworthiness and Maintenance, Civil Aviation University of China, Tianjin 300300, China

² Institut Clément Ader (ICA), CNRS, IMT Mines Albi, INSA, ISAE-SUPAERO, UPS, Université de Toulouse, Campus Jarlard, 81013 Albi, France

³ CIRIMAT, Université de Toulouse, CNRS, Université Toulouse 3 Paul-Sabatier, 118, Route de Narbonne, 31062 Toulouse Cedex 9, France

cracking and detrimental spallation of the protective YSZ deposit.

The adherence properties of TBC systems usually decrease following exposure at high temperature because of the in-service growth of a TGO (thermal grown oxide) layer, which is always a multi-scale oxide composed of one layer of Al_2O_3 and one layer of CoCrNiO , between the bond coat and the ceramic topcoat, combined with the development of residual stresses within the TBC at the interface between the various layers of different natures (Ref 3, 4). This TGO layer, acting as a diffusion barrier, generally exhibits roughly parabolic growth kinetics, until either out-of-plane or in-plane cracking develops, which stands as the onset of the degradation that usually develops through the detachment and ejection of TBC or TBC plus TGO particles. Consequently, this spallation-induced damage strongly limits the lifetime of the TBC systems. As a matter of fact, the interfacial toughness, indicating the ability of the system to resist to the initiation and propagation of cracks across the TGO, at the interface between the TGO and the topcoat or throughout the bond coat, is one of the most important factors to address for assessing TBC systems durability (Ref 5). In relation to various manufacturing processes and various aging conditions, several specific interfacial toughnesses and spallation locations in relationship with microstructural details such as TGO thickness, interfacial rumpling, barbules development, have been investigated (Ref 6, 7), including one of our previous work (Ref 8).

Because pre-spallation damages, as buckle, ridge or wedge formation, are insidious, photoluminescence methods are being developed for early detection and monitoring of TBC damages at the interface between the bond coat and the topcoat prior to the onset of the ceramic layer spalling (Ref 9, 10), so as to effectively avoid damage in combustion chamber and blades. Photoluminescence is a solid-state physics property related to the relaxation down to the ground state of electrons initially brought up to an excited state by the absorption of light. This results in radiative electronic transitions leading to a spontaneous emission of photons (Ref 11). The spectral and temporal characteristics of the luminescence emissions can be used to determine the critical temperature for material damages (Ref 9, 10, 12, 13). Photoluminescence methods, which rely on the functionalization of the topcoat with trivalent lanthanide ions with fluorescence properties, show high accuracy and stability (Ref 14, 15). Nowadays, YSZ layers doped with rare earth elements can be prepared at different depths in the ceramic topcoat by plasma spray to achieve nondestructive through-thickness testing of YSZ within the entire volume of the TBC, and especially close to the interface with the bond coat where most damage mechanisms occur.

Several researches have investigated the influence of the introduction of rare earth elements into ceramic coatings. While some detrimental effects of this introduction on the TBC were reported, it can as well improve some of the functional properties of TBCs. Leilei Sun et al. showed that the thermal conductivity of Yb_2O_3 and Y_2O_3 co-doped zirconia is 20% lower than that of standard YSZ (Ref 16). Other lanthanide ions such as Pr^{3+} , Nd^{3+} , Gd^{3+} , Dy^{3+} , Er^{3+} are also reported as efficient dopants to significantly reduce the thermal conductivity of ZrO_2 (Ref 17-21). Habibi et al. compared the hot corrosion performance of YSZ and TaYSZ ($\text{YSZ-Ta}_2\text{O}_5$) composite samples and showed that TaYSZ has much better hot corrosion resistance than YSZ in the presence of a molten mixture of $\text{Na}_2\text{SO}_4 + \text{V}_2\text{O}_5$ at 1100 °C (Ref 22). However, Pilgrim et al. (Ref 23) indicated that layers of YSZ:Dy^{3+} and YSZ:Eu^{3+} deposited by plasma spray exhibit higher erosion rate than undoped YSZ layers at 20 and 800 °C, as already observed at 20 °C on EB-PVD TBCs doped with 2-4 mol.% of Gd_2O_3 (Ref 24).

Because of their ionic radii close to that of Y^{3+} , the addition of lanthanides into the crystal structure of zirconia leads similarly to the stabilization of the quadratic t' or the cubic c structure. Jiang et al. (Ref 25) examined these phase transformations and lattice parameter change as a function of temperature by comparing YSZ, CeO_2 -doped YSZ and Nb_2O_5 -doped YSZ. Functionalization of TBC for photoluminescence applications generally requires small amounts of activators (1-3 mol.%), which are usually assumed to not disturb the integrity and properties of the coating. TBC luminescence sensing methods are intended to be used in particular for the monitoring of the damage in TBC during research and development phases, under the assumption that the behavior of the doped TBC is the same as that of a conventional TBC. Previous works from the authors (Ref 26) showed that even the introduction of small amounts of lanthanide ions in the lattice of YSZ (1-5 mol.%) produced by a sol-gel route, if not compensated by an equal reduction of the amount of Y^{3+} ions, can already lead to substantial modification of the lattice parameters. This leads to an increase of the tetragonality coefficient $c/a\sqrt{2}$ of the t' phase from the optimum value assumed to ensure the best thermo-mechanical properties. In the authors' opinion, there has been only little research conducted on the durability of functionalized TBC, especially about the impact of lanthanide doping on the interfacial toughness, an important factor regarding the quality and performance of TBC systems.

The objective of this paper is to investigate the influence of the functionalization of YSZ with 2 mol.% of $\text{EuO}_{1.5}$, especially on the interfacial toughness and the TGO morphology of APS TBC after long-term isothermal exposure at high temperature. Eu^{3+} is selected as it exhibits a bright

luminescence signal in YSZ coatings (Ref 26) and is often used for the production of TBC sensors (Ref 10, 12, 27-29). YSZ powder of composition $((YO_{1.5})_{0.098}(ZrO_2)_{0.902})$ and YSZ:Eu powder of composition $((EuO_{1.5})_{0.02}(YO_{1.5})_{0.078}(ZrO_2)_{0.902})$ are used to deposit two types of TBC systems constituted of a YSZ layer (undoped or Eu^{3+} -doped) on top of a CoCrAlY bond coat by using atmospheric plasma spray (APS) method. The main degradation of such multilayer system is due to an alteration of the adherence at the interfaces of the thermal barrier coating as a consequence of isothermal oxidation (Ref 30). Specimens are thus oxidized under isothermal conditions at 1100 °C up to 800 h in order to grow oxide layers with different thicknesses and different proportions of Al_2O_3 versus CoCrNiO. By using interfacial indentation test (Ref 31, 32), interfacial toughness of specimens relative to different aging treatments are analyzed. TGO morphology and composition are also derived from scanning electron microscopy (SEM) and energy dispersive x-ray spectroscopy (EDS), respectively.

Experimental

Preparation of Specimens

Substrates are cylinders with a diameter of 25.4 mm and a thickness of 6 mm. The substrate material is Hastelloy-X superalloy. CoCrAlY powders are used to prepare the bond coat, whose thickness is around 100 μm . This CoCrAlY powder is composed of 23 wt.% of chromium (Cr), 13 wt.% of aluminum (Al), 0.5 wt.% of yttrium (Y) and balance cobalt (Co). Two kinds of YSZ powders are used to deposit the topcoat, (1) undoped YSZ with typical equilibrium composition $(YO_{1.5})_{0.098}(ZrO_2)_{0.902}$ that guarantees the crystallization of the quadratic phase t' , (2) Eu-doped YSZ powder (YSZ:Eu) with composition $(EuO_{1.5})_{0.02}(YO_{1.5})_{0.078}(ZrO_2)_{0.902}$. Both kinds of powders are produced by Zhoushan Tengyu Aerospace New Material Co., Ltd., Zhejiang China. For the Eu-doped powder, the total amount of stabilizing elements ($EuO_{1.5}$ and $YO_{1.5}$) remains the same as for the undoped powder, so that the quadratic t' phase crystallizes with the same coefficient of tetragonality (Ref 26). These powders are used to deposit a 160 μm thick layer of ceramic topcoat by APS on the substrates with bond coat. Two types of APS specimens with different topcoats are prepared: (1) Type I with a topcoat made of YSZ:Eu powder, (2) Type II with a topcoat made of YSZ powder. The two types of coatings are illustrated in Fig. 1.

An APS 3710 model manufactured by PRAXAIR is used to prepare the TBCs, both for bond coat and topcoat. A six-axis robot automatic hand model 2400 M

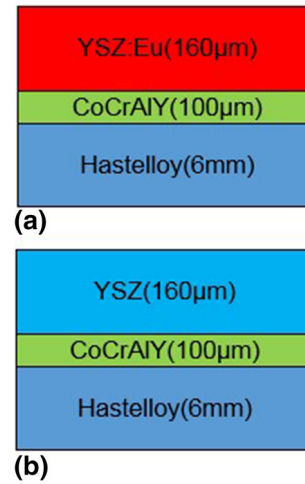


Fig. 1 Illustration of the different types of ASP YSZ coatings: (a) Type I (Eu^{3+} doped) (b) Type II (undoped)

Table 1 Parameters for preparing the APS CoCrAlY bond coat

| Item | Gas | Value |
|-----------------------------------|-----|-------|
| Primary gas/PSI | Ar | 60 |
| Secondary gas/PSI | He | 120 |
| Carrier gas/PSI | Ar | 40 |
| Current/A | | 835 |
| Voltage/V | | 38 |
| Spray distance/mm | | 85 |
| Gun moving velocity/ $mm\ s^{-1}$ | | 450 |
| Powder source speed/RPM | | 3.5 |

manufactured by ABB is used for spraying in order to ensure an accurate and consistent distance and projection speed. The spraying parameters for the bond coat and the topcoats are given in Tables 1 and 2, respectively:

Isothermal Heat Treatment of Specimens

Isothermal oxidation specimens are divided into three groups, all tested in the same furnace (CARBOLITE-CWF1300) and at the same temperature, i.e., 1100 °C. First, second and third group are, respectively, exposed during 100, 200 and 800 h. Following oxidation, all specimens from the three groups are compared to the as-deposited specimens.

Microstructure and Interfacial Toughness Characterization

The cross sections of the coated specimens are investigated by scanning electron microscopy (SEM) to reveal the details of the morphology, the possible damage and the

Table 2 Parameters for preparing the APS YSZ topcoats

| Item | Gas | Value |
|--|-----|-------|
| Primary gas/PSI | Ar | 60 |
| Secondary gas/PSI | He | 120 |
| Carrier gas/PSI | Ar | 30 |
| Current/A | | 860 |
| Voltage/V | | 38.7 |
| Spray distance/mm | | 72 |
| Gun moving velocity/mm s ⁻¹ | | 250 |
| Powder source speed/RPM | | 4.0 |

overall microstructure. The hardness and Young's modulus of the coatings (both of bond coats and topcoats) are deduced from measurements made on a CSM Indentation Tester equipped with a Berkovich nano-indenter. They are, respectively, derived from optical microscopy images and elastic force–displacement curves as shown for a given case of topcoat in Fig. 2(a) and (b). The principle of the measurement is based on the depth-controlled indentation of the material. Once the targeted penetration (2 μm in the case illustrated in Fig. 2b) is reached, the load is kept constant for a short time (under a force of 380 nN in the case illustrated in Fig. 2b), giving rise to a slight material relaxation. The force is then released to retrieve the elastic strain produced by the indentation. After measuring the size of the indent imprint and the slope of the elastic curve upon stress release, the Vickers hardness and Young's modulus are, respectively, calculated automatically.

For bi-materials, a simple model basically based on a mixing law to quantitatively estimate the apparent toughness of the interface is proposed in Ref. 33 for hard coatings. It is shown that the apparent interfacial toughness (K_{ca}) can be calculated using the following equation:

$$K_{ca} = 0.015 \frac{P_c}{a_c^{3/2}} \left(\frac{E}{H} \right)_i^{1/2} \quad (\text{Eq 1})$$

where H is the hardness, E the elastic modulus (subscript I stands for Interface), P_c is the critical value (in Newton) of the load P exerted using Vickers indentation at the interface between the two materials of the system and a_c is the critical crack size (in m). Both P_c and a_c correspond to the critical values of load and crack size, respectively, related to the onset of interfacial crack initiation due to indentation.

The value of the ratio $\left(\frac{E}{H}\right)_I^{1/2}$ relative to the interface between the bond coat and the topcoat is given by Eq. (2):

$$\left(\frac{E}{H} \right)_I^{1/2} = \frac{\left(\frac{E}{H} \right)_S^{1/2}}{1 + \left(\frac{H_S}{H_{TC}} \right)^{1/2}} + \frac{\left(\frac{E}{H} \right)_{TC}^{1/2}}{1 + \left(\frac{H_{TC}}{H_S} \right)^{1/2}} \quad (\text{Eq 2})$$

where subscripts S and TC stand for substrate (bond coat) and topcoat (ceramic layer), respectively.

The methodology to measure the various parameters included in the above model and derive experimental values of the interfacial toughness has been extensively introduced and discussed in Ref 34. Note that the method employs a pyramidal indenter and can be applied for a large range of coating thicknesses (greater than 100 μm); it is specifically used for investigating adhesion of TBC systems (Ref 35). Basically, for one specimen corresponding to a given aging condition, each interfacial indentation load P generates a square-shaped indent imprint with diagonal b and, if any (when $P \geq P_c$), a crack with size a ($a \geq a_c$). Four to five indentations are performed for each load to be as representative as possible and to minimize error. Quantitative approach is derived by plotting two lines, i.e., $\ln(P)$ versus $\ln(b)$ (*master curve*) and $\ln(P)$ versus $\ln(a)$ (*crack curve*). The intercept between the two curves simply gives the critical load P_c and the critical crack size a_c . The values of a and b are measured from SEM micrographs as shown in Fig. 3.

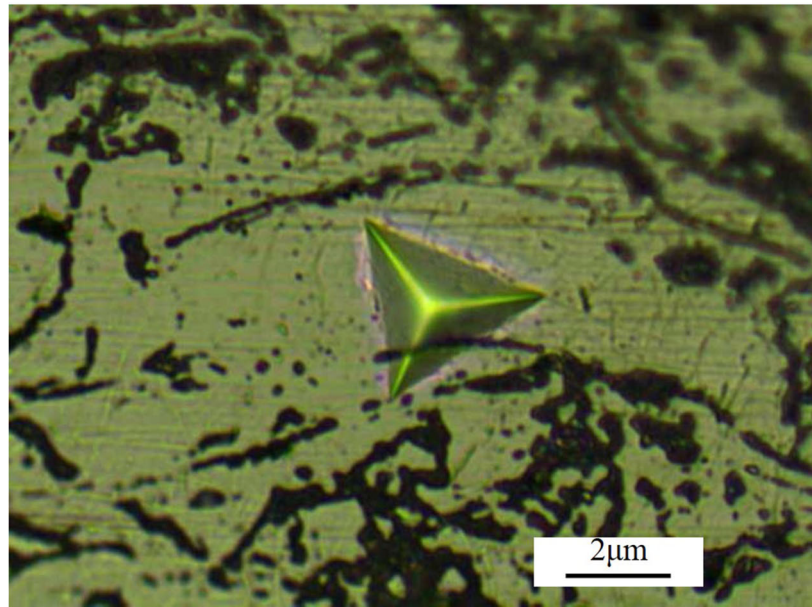
Results and Discussion

Interfacial Toughness

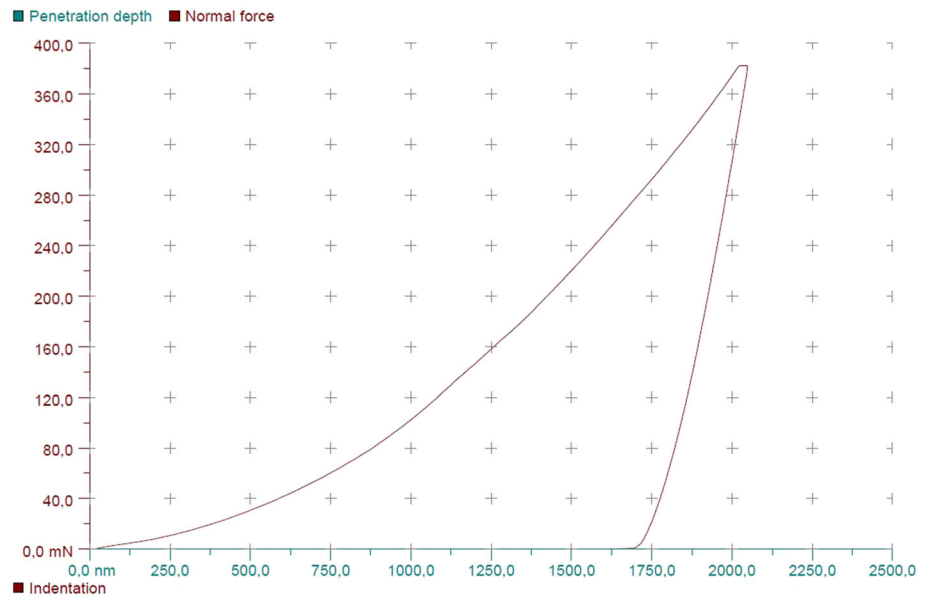
Hardness and Young's modulus values of both the bond coat and the topcoat for the two types of coatings are shown in Table 3. They are, respectively, 585 ± 5 HV and 73.7 ± 2.1 GPa for the doped topcoat, and 587 ± 3 HV and 73.5 ± 3.6 GPa for the undoped topcoat. These values fall in the expected range of hardness and Young's modulus for typical dense APS TBCs (300-700 HV and 75 GPa), as indicated in Ref 36. It is concluded that the hardness and stiffness of Type I and Type II TBCs are very similar, indicating that the addition of 2 mol.% of Eu^{3+} ions in substitution to Y^{3+} ions does not modify the HV and E values of the YSZ topcoat.

Plotted in Fig. 4 with square-shaped symbols is the curve gathering the whole set of indent diagonal b data obtained for the whole bunch of specimens, respectively, aged and non-aged, the so-called master curve as defined above in part 2.3. The satisfactorily fitted linear relationship between $(\ln b)$ and $(\ln P)$, showing slopes close to 0.5 (0.537 and 0.547 for coatings Type I and Type II, respectively, see Table 4), is in good agreement with the general standard formula relating the Vickers hardness (HV) of bulk materials to the ratio between the applied load P and the square of the diagonal length b^2 , as discussed in Ref. (Ref 34). This master curve corresponds to typical hardness curve, its slope (close to 0.5) is independent of the

Fig. 2 (a) Berkovich nano-indentation imprint (b) Load-penetration and relaxation curve on the topcoat



(a)

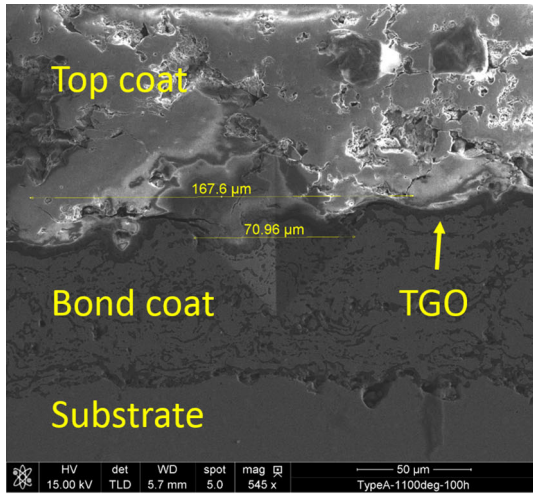


(b)

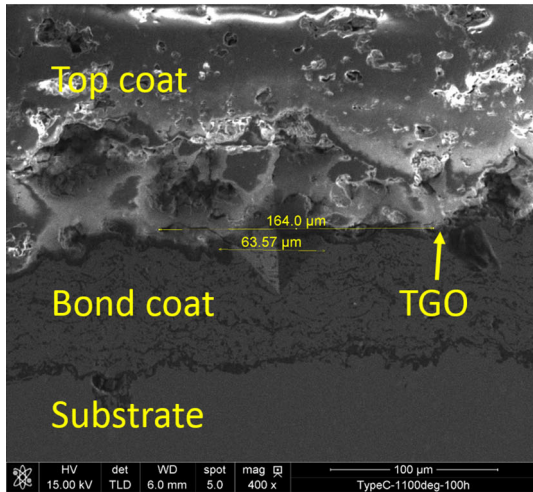
aging conditions. It is also checked that its position does not depend on the holding time. Both conditions justify plotting all values on a same graph.

Crack curves representing the evolution of the load-induced crack length for the various oxidation conditions tested, ($\ln a$) versus ($\ln P$), are superimposed to the master curve in Fig. 4. Note that for a given oxidation time and temperature, that is for a given oxide thickness, the variation of the length a of the indentation-induced crack versus the applied load P also fits a single regression line in a Log-Log scale. The intercept between the

master curve and crack curves, giving the critical load, discriminates the two domains where the applied load is, respectively, (1) too low to initiate interfacial cracking, (2) high enough to provoke the initiation and the propagation of an interfacial crack. Note that the required force for the onset of crack formation decreases with the aging time. This is straightforwardly related to the increasing density of structural interfacial defects as the interfacial TGO grows. These defects are prone to preferentially initiate cracking as a result of possible local stress concentration.



(a)



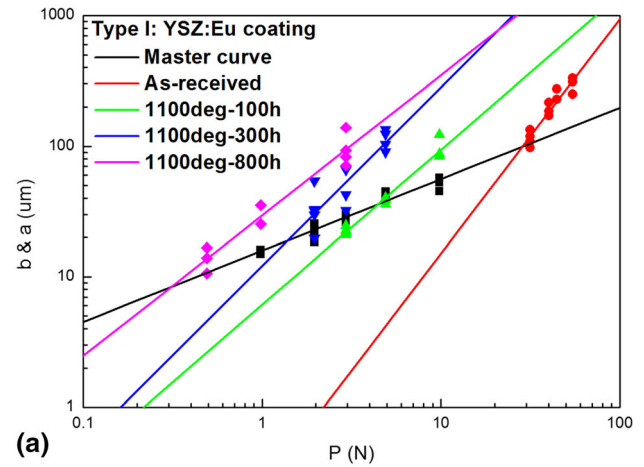
(b)

Fig. 3 Principle for measuring $2a$ (crack size) and $2b$ (indentation imprint size) by scanning electron microscopy (in case of 9.8 N of load P)

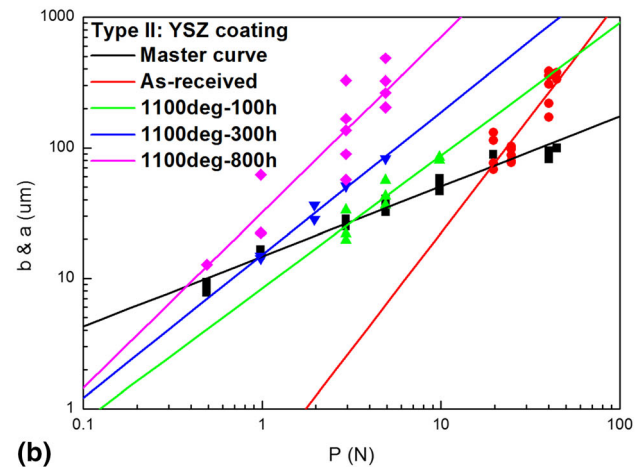
Table 3 Values of hardness and Young's modulus measured by nano-indentation (Berkovich)

| Layer | Hardness, HV | Young's modulus, GPa |
|-------------------|--------------|----------------------|
| Type I-topcoat | 585 ± 5 | 74 ± 3 |
| Type II-topcoat | 587 ± 3 | 74 ± 4 |
| Type I-bond coat | 485 ± 4 | 126 ± 5 |
| Type II-bond coat | 485 ± 6 | 126 ± 6 |

For the cases shown in Fig. 4, Table 4 gives the correlation when fitting the experimental data points with a linear model (slope and regression coefficient). Most plots give satisfactory correlation. However, note that some regression coefficients are lower than 0.9, which is directly



(a)



(b)

Fig. 4 Graphical determination of critical loads causing interfacial cracking of thermal barriers coatings: (a) Type I: YSZ:Eu coating and (b) Type II: YSZ coating

Table 4 Equations of linear master curve and crack curves for various exposure times at 1100 °C

| Conditions | Equations | Linearity |
|----------------------|--------------------------------|-----------|
| Type I-Master curve | $\ln(b) = 0.547\ln(P) + 2.765$ | 0.941 |
| Type II-Master curve | $\ln(b) = 0.537\ln(P) + 2.688$ | 0.966 |
| Type I as-deposited | $\ln(a) = 1.795\ln(P) - 1.419$ | 0.882 |
| Type II as-deposited | $\ln(a) = 1.783\ln(P) - 1.000$ | 0.834 |
| Type I-100 h | $\ln(a) = 1.187\ln(P) + 1.812$ | 0.968 |
| Type II-100 h | $\ln(a) = 1.017\ln(P) + 2.126$ | 0.880 |
| Type I-300 h | $\ln(a) = 1.410\ln(P) + 2.404$ | 0.786 |
| Type II-300 h | $\ln(a) = 1.094\ln(P) + 2.716$ | 0.981 |
| Type I-800 h | $\ln(a) = 1.076\ln(P) + 3.385$ | 0.933 |
| Type II-800 h | $\ln(a) = 1.344\ln(P) + 3.467$ | 0.807 |

related to the dispersion in crack size measured after indentation, as illustrated in Fig. 3. As a matter of fact, in as-deposited specimens with no TGO, the preferential

crack path is not always confined along the interface but sometimes deviates locally within the topcoat resulting in some dispersion (see Fig. 3). In aged specimens with TGO, the heterogeneity of the interfacial tortuosity gives also some heterogeneity in crack length.

Values for the critical load P_c , the critical crack size a_c , the apparent toughness K_{ca} and the oxide thickness ζ are given in Table 3. As expected, for both Type I and Type II coatings, the critical load to efficiently indent the interface between the CoCrAlY bond coat and the YSZ topcoat and subsequently produce a measurable interfacial crack, decreases with the severity of the high temperature exposure, i.e., the exposure time, resulting in a decrease in the interfacial toughness (Table 5 and Fig. 5). The interfacial toughness decreases from 1.9 ± 0.3 and 2.1 ± 0.4 MPa m^{-1/2} for the as-deposited coating to 0.84 ± 0.08 and 0.8 ± 0.2 MPa m^{-1/2} after 800 h at 1100 °C, respectively, for Type I and Type II coatings. Given the experimental uncertainties determined, it can be concluded that statistically there is no difference between the interfacial toughness of the two types of coatings

Table 5 Critical load P_c , critical crack size a_c , interfacial toughness K_{ca} and TGO thickness ζ for various exposure times at 1100 °C

| Conditions | P_c , N | a_c , μm | K_{ca} , MPa m ^{1/2} | ζ , μm |
|----------------------|-----------|-----------------------|---------------------------------|-------------------------|
| Type I as-deposited | 28.56 | 99.35 | 1.9 ± 0.3 | 0 |
| Type II as-deposited | 19.22 | 71.59 | 2.1 ± 0.4 | 0 |
| Type I-100 h | 4.45 | 35.92 | 1.4 ± 0.2 | 9 ± 4 |
| Type II-100 h | 3.22 | 27.50 | 1.5 ± 0.2 | 10 ± 3 |
| Type I-300 h | 2.01 | 23.28 | 1.1 ± 0.3 | 12 ± 4 |
| Type II-300 h | 0.95 | 14.30 | 1.16 ± 0.05 | 12 ± 4 |
| Type I-800 h | 0.31 | 8.28 | 0.84 ± 0.08 | 20 ± 8 |
| Type II-800 h | 0.30 | 8.76 | 0.8 ± 0.2 | 18 ± 8 |

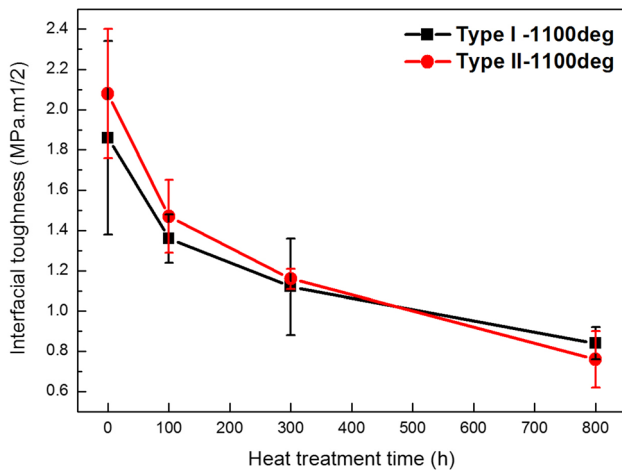


Fig. 5 Evolution of the interfacial toughness as a function of the holding time at 1100 °C for Type I and Type II TBCs

whatever the exposure time is, i.e., the substitution of 2 mol.% of Y³⁺ ions by Eu³⁺ ions does not alter the capacity of the interface to resist to cracking from one APS TBC system to the other. After a significant drop between 0 and 100 h of aging, the further decrease in interfacial toughness occurs at a relatively smooth and constant rate. This similar decrease is the result of the similar growth of the TGO in both cases, leading to similar decrease in critical crack length of the damage containing TGO layer for both types of coatings during the heat exposure (up to 9 ± 4 and 10 ± 3 μm , as discussed in the next section).

TGO Morphology

Results from Table 5 shows that the interfacial toughness decreases as TGO thickness increases. The TGO thicknesses are measured from SEM images showing the interfacial morphologies as illustrated in Fig. 6 for Type I coatings in as-deposited and aged conditions. Note that the morphologies for Type II coatings, not shown here, are very similar. In addition to the TGO thickening, micrographs reveal the presence of porosity, micro-cracks and local thickness heterogeneity whose amount increases with aging time. EDS analyses of a representative TGO grown 300 h at 1100 °C are presented in Fig. 6. The TGO is composed of one dark-contrast layer (analyzed in Point 1) and one bright-contrast layer (Point 2), an observation already reported in the previous work (Ref 8). The EDS (energy dispersive spectroscopy) results (Fig. 7b and c) indicate that the main components of the darkest layer are aluminum and oxygen (likely to be Al₂O₃) and that of the brightest layer are Co and Cr corresponding to a complex CoCr oxide in addition to Al₂O₃. EDS results also show that there is no Eu³⁺ diffusion into neither the Al₂O₃ nor the Co/Cr/Al₂O₃ layer, as Eu³⁺ can only be detected in the ceramic coating as expected (Fig. 7d).

Figure 8 plots the variation of TGO thickness with high temperature exposure time, which follows roughly parabolic growth kinetics. There is no statistical difference between the TGO growth in Type II undoped coatings and Type I YSZ:Eu coatings. The TGO thickness is comprised between 9 and 10 μm after 100 h at 1100 °C, around 12 μm after 300 h, and between 18 and 20 μm after 800 h.

The large uncertainties observed for the longest exposure time are related to the local thickness heterogeneities discussed in the previous paragraphs. It is assumed that these heterogeneities also explain the difference in the slopes between the as-deposited and the aged crack curve shown in Fig. 4.

By plotting the evolution of crack length a produced by indentation versus the applied load P , an attempt is made to define a factor indicating the sensitivity of cracking to the indentation force to address the detrimental effect of these

Fig. 6 TGO morphologies of Type I coating for different isothermal oxidation conditions: (a) as-deposited (b) 1100 °C-100 h (c) 1100 °C-300 h (d) 1100 °C-800 h

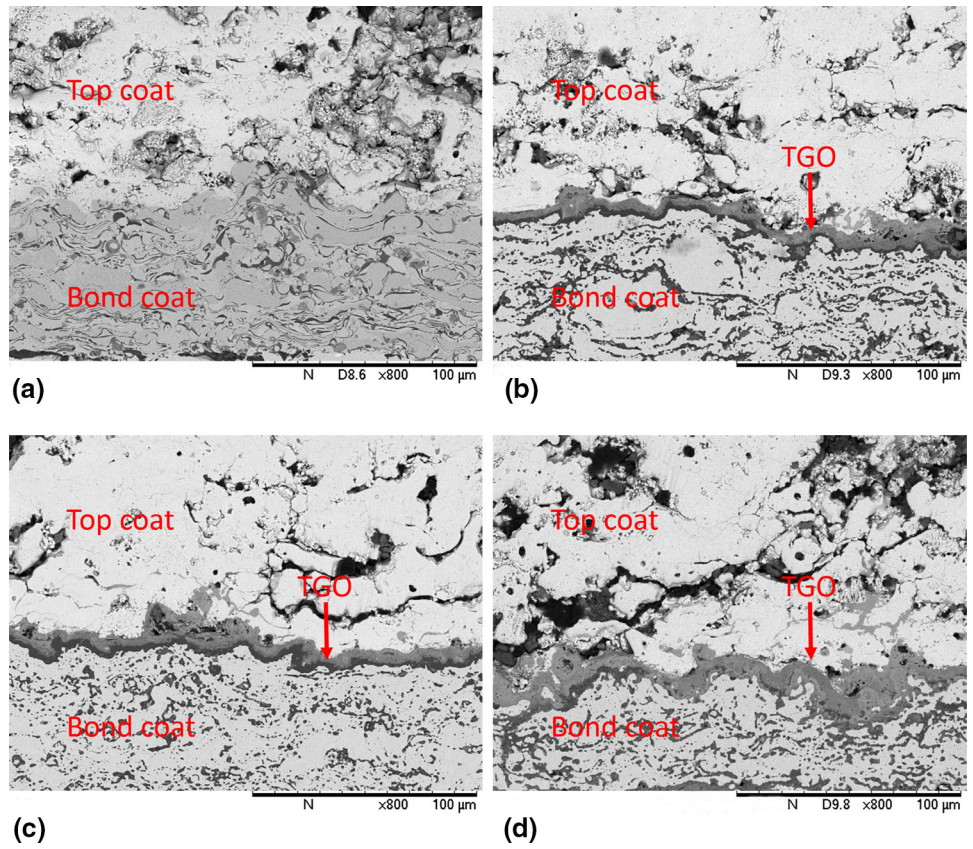
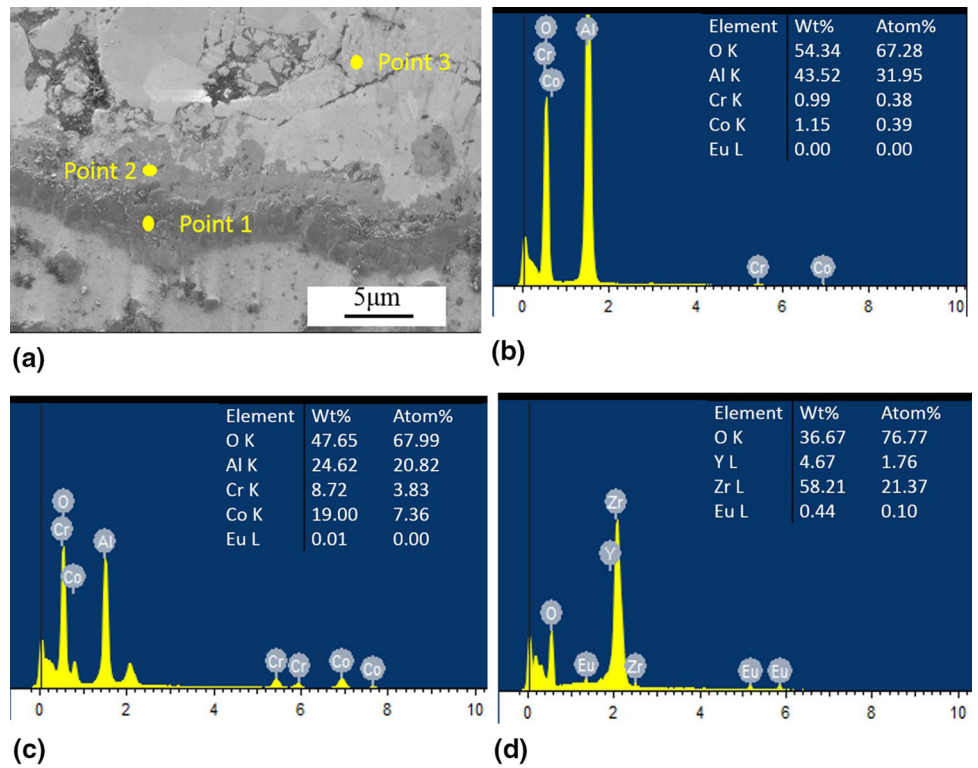


Fig. 7 (a) Type I: 1100°-300 h (b) EDS peaks in Point 1 (c) EDS peaks in Point 2 (d) EDS peaks in Point 3



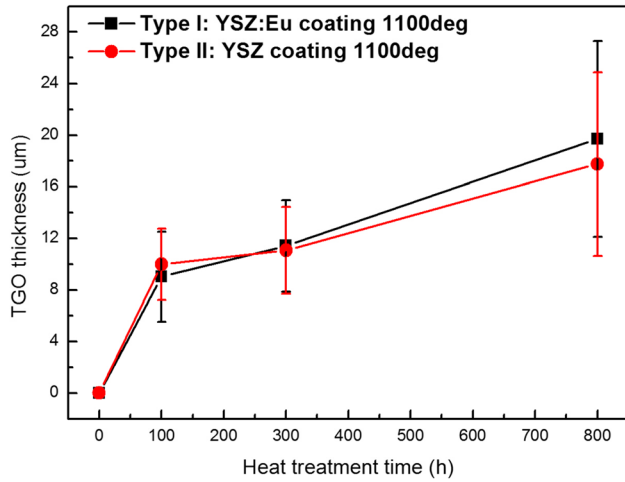


Fig. 8 Evolution of the oxide thickness as a function of aging time at 1100 °C

heterogeneities. This coefficient s revealing the load sensitivity of the crack propagation ($LSCP$) is tangential to the curve at each point. It can be calculated as the differential da/dP of the curve and is expressed in micrometers per newton. It comes:

$$S = \frac{da}{dP} \quad (\text{Eq 3})$$

In all aging conditions investigated for Type I and Type II thermal barrier coatings and considering for each case the explored domain of load, it is shown that the variation of the mean crack length with indentation force is satisfactorily approximated using a linear model with regression coefficients ranging from 0.94 to 0.99. This suggests that, at least in the load range investigated, the coefficient s of load sensitivity of the crack propagation does not depend on the indentation force and can be simply derived from the slopes of the experimental plots. Consequently, s can be written as:

$$S = \frac{\Delta a}{\Delta P} \quad (\text{Eq 4})$$

Figure 9 shows the evolution of s as a function of the aging condition for both Type I and Type II TBCs. Coefficient s globally exhibits a monotonous increase as the aging time extends. This suggests that the multilayered TBC systems are progressively more sensitive to the indentation load when the interfacial TGO between the bond coat and the topcoat further thickens and damages through the occurrence of structural defects while growing. A large dispersion for s is, however, shown for the longest aging time, which is 800 h, in direct relation with the large dispersion in measured crack length values. In addition, note that values of s are very similar for Type I and Type II TBCs, even for the 800 h aging condition where the error

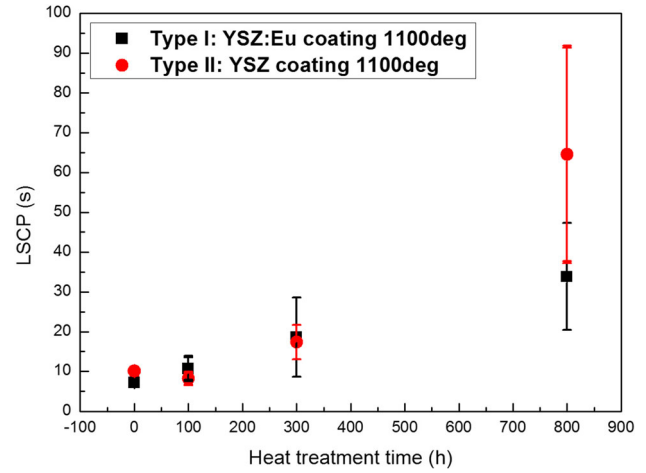


Fig. 9 Load sensitivity of crack propagation ($LSCP$) versus aging time

bars of the two types slightly superimpose, indicating as well that the presence of dopant elements incorporated in the barriers does not impair the load sensitivity coefficient whatever the aging time is. This is also very consistent with the associated decrease in the interfacial toughness detailed in Fig. 5.

According to the scanning electron microscopy observations and mechanical properties results, there is almost no difference between the doped (Type I) and the non-doped (Type II) TBC systems in terms of initial Young's modulus and hardness, values and evolution of interfacial toughness, overall microstructure and interfacial morphology. This can be explained considering the small amount of rare earth elements in the functional coating (2 mol.%) incorporated in substitution to Y^{3+} ions. Since the properties of the YSZ remain the same [structure lattice (Ref 26), hardness and Young's module] and because the Eu^{3+} does not impact the growth of the TGO (no diffusion of Eu^{3+} ions, and no difference in growth rate and defect density), no difference is observed in interfacial toughness, which is mainly controlled by the TGO characteristics for the coating systems presented here, which keep unchanged the total amount of stabilizing element ($Y^{3+} + Eu^{3+} = 9.8$ mol.%). Used as luminescent markers for temperature and damage diagnostic in TBCs, it is expected that Eu^{3+} ions will not contribute to any kind of degradation of the coating durability through spallation.

Conclusion

The main objective of this paper was to study the influence of small rare earth element additions (Eu^{3+}) on interfacial toughness and TGO morphology of APS YSZ TBCs. The interfacial toughness and TGO morphology of undoped

YSZ and YSZ:Eu³⁺ (2 mol.%) coatings after 100 h-800 h exposure at 1100 °C under isothermal conditions were investigated.

According to the interfacial toughness results, there is statistically no difference between Eu-doped coatings and undoped coatings regarding microstructural characteristics and mechanical properties. For both types of coatings, the indentation tests showed that the oxidation of the bond coat, leading to an increase in the thermally grown oxide (TGO) thickness, consistently resulted in a decrease of the toughness of the interface between the bond coat and the topcoat. Concomitantly, the coefficient of load sensitivity of the crack propagation (*LSCP*), calculated as the slope of the linear plots relating crack length to indentation force is similar for both types of coatings and increases as the aging time increases in relationship with the associated interfacial degradation.

These results are explained by the following elements:

- The substitution of only 2 mol.% of Y³⁺ by Eu³⁺ ions, also a stabilizing element for the *t'* phase of ZrO₂, does not modify significantly the crystalline structure and the mechanical properties of the YSZ topcoat (mainly hardness and modulus of elasticity).
- The Eu³⁺ ions do not diffuse into the TGO layer at the interface and consequently do not alter the TGO growth kinetics and morphology, which remain similar for both types of coatings.
- The measured decrease in interfacial toughness and increase in the coefficient of load sensitivity of the crack propagation (*LSCP*) are mainly controlled by the growth of the TGO layer, its morphology and its structural defects.

As small Eu³⁺ additions in substitution to Y³⁺ in APS-YSZ coatings have no influence on their interfacial toughness, it is therefore concluded that this kind of doped coatings are promising candidates for investigating and monitoring damage using photoluminescence methods. Work is in progress to check the feasibility and efficiency of using Eu³⁺ functionalization as a nondestructive testing route to perform in situ real time monitoring of APS YSZ TBCs and correlate luminescence signals to structural damage occurrence and evolution (Ref 9-13). In the future, the effect of such addition elements on other mechanical properties (such as erosion for instance) will be checked.

Acknowledgments This work was financially supported by the projects of Civil Aviation Authority Science and Technology Program (MHRD20160106), Central University Basic Scientific Research Operation Cost Special Fund of Civil Aviation University of China (3122018D032). The support of the Ecole Doctorale – Aéronautique Astronautique (ED 467), Toulouse France, is also gratefully acknowledged. Thanks to Keyurbhai Maniya, intern of Institut

Clément Ader in Mines Albi and Liping Yang, master student of Civil Aviation University of China for their help during the experiment.

References

1. N. Padture, M. Gell, and E.H. Jordan, Thermal Barrier Coatings for Gas-Turbine Engine Applications, *Science*, 2002, **296**, p 280-284
2. B. Goswami, K.R. Ashok, and S.K. Sahay, Thermal Barrier Coating System for Gas Turbine Application—A Review, *High Temp. Mater. Process.*, 2004, **23**, p 73-92
3. W.R. Chen, X. Wu, and D. Dudzinski, Influence of Thermal Cycle Frequency on the TGO Growth and Cracking Behaviors of an APS-TBC, *J. Therm. Spray Technol.*, 2012, **21**(6), p 1294-1299
4. M. Gupta, K. Skogsberg, and P. Nylén, Influence of Topcoat-Bondcoat Interface Roughness on Stresses and Lifetime in Thermal Barrier Coatings, *J. Therm. Spray Technol.*, 2014, **23**(1-2), p 170-181
5. W.R. Chen, R. Archer, X. Huang et al., TGO Growth and Crack Propagation in a Thermal Barrier Coating, *J. Therm. Spray Technol.*, 2008, **17**(5-6), p 858-864
6. L. Pin, V. Vidal, F. Blas, F. Ansart, S. Duluard, J.P. Bonino, Y. Le Maoult, and P. Lours, Optimized Sol-Gel Thermal Barrier Coatings for Long-Term Cyclic Oxidation Life, *J. Eur. Ceram. Soc.*, 2014, **34**, p 961-974
7. J. Sniezewski, V. Vidal, P. Lours, and Y. Le Maoult, Thermal Barrier Coatings Adherence and Spallation: Interfacial Indentation Resistance and Cyclic Oxidation Behavior Under Thermal Gradient, *Surf. Coat. Technol.*, 2009, **204**, p 807-811
8. Y.K. Liu, Y.H. Liu, P. Lours et al., Influence of Isothermal Aging Conditions on APS TBC's Interfacial Fracture Toughness, *Surf. Coat. Technol.*, 2017, **313**, p 417-424
9. J.I. Eldridge and T.J. Bencic, Monitoring Delamination of Plasma-Sprayed Thermal Barrier Coatings by Reflectance-Enhanced Luminescence, *Surf. Coat. Technol.*, 2006, **201**, p 3926-3930
10. J.I. Eldridge, T.J. Bencic, C.M. Spuckler, J. Singh, and D.E. Wolfe, Delamination-Indicating Thermal Barrier Coatings Using YSZ: Eu Sublayers, *J. Am. Ceram. Soc.*, 2006, **89**, p 3246-3251
11. C. Pilgrim, S. Berthier, J. Feist et al., Photoluminescence for Quantitative Non-destructive Evaluation of Thermal Barrier Coating Erosion, *Surf. Coat. Technol.*, 2012, **209**(9), p 44-51
12. M.M. Gentleman and D.R. Clarke, Concepts for Luminescence Sensing of Thermal Barrier Coatings, *Surf. Coat. Technol.*, 2004, **188**, p 93-100
13. R.J.L. Steenbakker, J.P. Feist, R.G. Wellman, and J.R. Nicholls, Sensor Thermal Barrier Coatings: Remote In Situ Condition Monitoring of EB-PVD Coatings at Elevated Temperatures, *J. Eng. Gas Turbines Power Trans.*, 2009, **131**, p 041301
14. G. Portu, L. Micele, Y. Sekiguchi et al., Measurement of Residual Stress Distributions in Al₂O₃/3Y-TZP Multilayered Composites by Fluorescence and Raman Microprobe Piezo-Spectroscopy, *Acta Mater.*, 2005, **53**(5), p 1511-1520
15. Y. Zhao, C. Ma, F. Huang et al., Residual Stress Inspection by Eu³⁺ Photoluminescence Piezo-Spectroscopy: An Application in Thermal Barrier Coatings, *J. Appl. Phys.*, 2013, **114**(7), p 502
16. L.L. Sun, H.B. Guo, H. Peng et al., Phase Stability and Thermal Conductivity of Ytterbia and Yttria Co-doped Zirconia, *Prog. Nat. Sci. Mater. Int.*, 2013, **23**(4), p 440-445
17. J.R. Nicholls, K.J. Lawson, A. Johnstone, and D.S. Rickerby, Methods to Reduce the Thermal Conductivity of EB-PVD TBCs, *Surf. Coat. Technol.*, 2002, **151**, p 383-391

18. D.S. Rickerby, P. Morrell, and Y.A. Tamarin, Metallic Article Having a Thermal Barrier Coating and a Method of Application Thereof, brevet US6025078 (A), 2000
19. M.J. Maloney, Thermal Barrier Coating Systems and Materials, brevet US6177200 (B1), 2001
20. U. Schulz, K. Fritscher, C. Leyens, M. Peters, and W.A. Kaysser, Thermocyclic Behavior of Differently Stabilized and Structured EB-PVD Thermal Barrier Coatings, *Mater. Werkst.*, 1997, **28**, p 370-376
21. U. Schulz, P. Moretto, B. Saint-Ramond, A. Vanlieshout, O. Lavigne, and A. Börger, Low Thermal Conductivity Ceramics for Turbine Blade Thermal Barrier Coating Application. In: E. Lara-Curzio, M.J. Readey (eds.) 28th International Conference on Advanced Ceramics and Composites B Engineering Science Proceedings. Wiley, 2004, p 375-380
22. M.H. Habibi, L. Wang, J.D. Liang et al., An Investigation on Hot Corrosion Behavior of YSZ-Ta₂O₅ in Na₂SO₄ + V₂O₅ Salt at 1100 °C, *Corros. Sci.*, 2013, **75**, p 409-414
23. C.C. Pilgrim, S. Berthier, J.P. Feist, R.G. Wellman, and A.L. Heyes, Photoluminescence for Quantitative Non-destructive Evaluation of Thermal Barrier Coating Erosion, *Surf. Coat. Technol.*, 2012, **209**, p 44-51
24. R.J.L. Steenbakker, R.G. Wellman, and J.R. Nicholls, Erosion of Gadolinia Doped EB-PVD TBCs, *Surf. Coat. Technol.*, 2006, **201**, p 2140-2146
25. S. Jiang, X. Huang, Z. He et al., Phase Transformation and Lattice Parameter Changes of Non-trivalent Rare Earth-Doped YSZ as a Function of Temperature, *J. Mater. Eng. Perform.*, 2018, **27**(5), p 2263-2270
26. E. Copin, T. Sentenac, Y. Le Maoult, F. Blas, F. Ansart, V. Vidal, and P. Lours, Feasibility of Luminescent Multilayer Sol-Gel Thermal Barrier Coating Manufacturing for Future Applications in Through-Thickness Temperature Gradient Sensing, *Surf. Coat. Technol.*, 2014, **260**, p 90-96
27. J.I. Eldridge, T.J. Bencic, S.W. Allison, and D.L. Beshears, Depth-Penetrating Temperature Measurements of Thermal Barrier Coatings Incorporating Thermographic Phosphors, *J. Therm. Spray Technol.*, 2004, **13**, p 44-50
28. M.D. Chambers, D.R. Clarke, Doped Oxides for High-Temperature Luminescence and Lifetime Thermometry. In: Annual Review of Materials Research, Palo Alto, 2009, p 325-359
29. M.M. Gentleman, J.I. Eldridge, D.M. Zhu, K.S. Murphy, and D.R. Clarke, Non-contact Sensing of TBC/BC Interface Temperature in a Thermal Gradient, *Surf. Coat. Technol.*, 2006, **201**, p 3937-3941
30. H.M. Tawancy, N. Sridhar, and N.M. Abbas, Failure Mechanism of a Thermal Barrier Coating System on a Nickel-Base Superalloy, *J. Materi. Sci.*, 1998, **33**, p 681-686
31. J.L. Vasinonta and A. Beuth, Measurement of Interfacial Toughness in Thermal Barrier Coating Systems by Indentation, *Eng. Fract. Mech.*, 2001, **68**, p S843-S860
32. W.G. Mao, J. Wan, C.Y. Dai et al., Evaluation of Microhardness, Fracture Toughness and Residual Stress in a Thermal Barrier Coating System: A Modified Vickers Indentation Technique, *Surf. Coat. Technol.*, 2012, **206**, p 4455-4461
33. D. Chicot, P. Démarécaux, and J. Lesage, Apparent Interface Toughness of Substrate and Coating Couples from Indentation Tests, *Thin Solid Films*, 1996, **283**, p 151-157
34. Y. Liu, V. Vidal, S. Le Roux, F. Blas, F. Ansart, and P. Lours, Influence of Isothermal and Cyclic Oxidation on the Apparent Interfacial Toughness in Thermal Barrier Coating Systems, *J. Eur. Ceram. Soc.*, 2015, **35**, p 4269-4275
35. L.T. Wu, R.T. Wu, X. Zhao, and P. Xiao, Microstructure Parameters Affecting Interfacial Adhesion of Thermal Barrier Coatings by the EB-PVD Method, *Mater. Sci. Eng. A*, 2014, **594**, p 193-202
36. P. Planques, V. Vidal, P. Lours et al., Mechanical and Thermophysical Properties of Plasma-Sprayed Thermal Barrier Coatings: A Literature Survey, *Oxid. Met.*, 2017, **88**, p 133-143

Publisher's Note Springer Nature remains neutral with regard to jurisdictional claims in published maps and institutional affiliations.